RSC Advances

ROYAL SOCIETY OF CHEMISTRY

www.rsc.org/advances

Development of long lifetime cathode materials for microplasma application

Srinivasu Kunuku,[a] Kamatchi Jothiramalingam Sankaran,[b] Chung-Li Dong,[c] Nyan-Hwa Tai,[b]

Keh-Chyang Leou,[a*] and I-Nan Lin,[d*]

Abstract: In this paper we are presenting the growth of three kinds of diamond films including ultrananocrystalline diamond (UNCD), nitrogen doped UNCD and hybrid granular structured diamond (HiD) films on Au coated silicon for applying as cathode in a parallel-plate type microplasma device. The phase constituents and microstructures of these diamond films were investigated in order to understand the role of intrinsic properties of these cathode materials on manipulation of the plasma characteristics of the corresponding devices. We observed that, while the diamond materials with high fraction of sp^2-bonded carbons exhibited the superior electron field emission (EFE) properties and hence the better plasma illumination (PI) behavior, the cathode materials with proper microstructure are required to ensure longer lifetime for practical applications of the microplasmas devices. Based on these observations, we have developed hybrid granular structured diamond films, in which the sp^2-bonded carbons were hidden in the boundaries between the sp^3-bonded diamond grains, such that the films exhibited not only excellent EFE properties and PI behavior but also good PI behavior with long lifetime.

Keywords: *diamond films, microplasma, lifetime, electron field emission, scanning microscopy, Raman spectroscopy, transmission electron microscopy*

Introduction

Microplasmas are gas discharges in small confined regions, which have potential applications in various fields such as ozone production for air cleaning,[1] surface treatment of materials for enhancing the wetting and adhesion properties of polymers,[2] highly efficient excimer ultra-violet (UV) light sources, plasma display panels,[3–7] and CO_2 lasers.[8–10] Recently, microplasmas are employed in the field of biotechnology for biological decontamination, sterilization and diffuse discharges.[11–14] Microplasma devices were successfully utilized in the fabrication of nanomaterials.[15,16] Development of atmospheric pressure microplasmas have great potentials for material synthesis, processing and material modifications for bio related applications[17–20]. Previous studies on cylindrical microplasma devices had shown broad range of operating parameters.[21–23] The electrode materials employed in micro-discharges are one of the key factors to sustain the high density plasmas at various pressures for long lifetime. Many different types of materials have been successfully applied as electrodes in microplasmas, ranging from refractive metals to semiconductors.[24–31] Due to ease of micro fabrication of Si, it was the most favorable material as electrode in microplasma applications.[32–37] In case of microplasma applications at high pressures, we need the electrode materials with high melting point materials such as molybdenum, alumina and boron nitride for operating at high temperature.[38,39] However, to sustain the plasma discharges, cathode materials with large secondary electron emission coefficient (γ-coefficient) are needed.[40] Diamond is the potential replacement of other materials as cathode due to its excellent physical and chemical properties such as wide bandgap, highest hardness, pronounced thermal conductivity, tunable negative electron affinity, high chemical inertness and most importantly the high

γ-coefficient.[41–46] Diamond films possessing superior electron field emission (EFE) properties and can supply electrons more efficiently has been observed to enhance the plasma illumination (PI) behavior of the microplasma devices.[47-50] Integration of diamond with CNT's, and different granular structure diamond films employed in order to enhance the microplasma characteristics[51–53] . On the other hand, high hardness and chemical inertness are the other features necessary to improve the robustness of cathode materials in microplasma devices. To achieve these characteristics simultaneously, microstructure for diamond films has to be developed properly.

In this study we had grown three kinds of diamond films with different granular structures for applying as the cathodes in the microplasma devices and systematically investigated their effect on the stability of the devices. The three different granular structures are ultrananocrystalline diamond (UNCD) films consisting of equi-axed ultra-small spherical grains[54], nitrogen doped UNCD (N-UNCD) films existing with acicular needle like granular structure[55] and hybrid granular diamond (HiD) films containing large diamond aggregates evenly dispersed in a matrix of nano-sized diamond grains[56]. We observed that diamond films with needle-like granular structure, which contains high fraction of sp^2-bonded carbon, possessing good EFE properties and superior PI behavior for the corresponding microplasma devices, but with inferior lifetime. Moreover, we found out that the hybrid granular structure diamond films, which have sp^2-bonded carbon embedded in sp^3-bonded diamond grains, showed not only marvelous EFE properties and hence superior PI behavior, but also exhibit excellent robustness.

Experimental Methods

The diamond deposition on Si substrate started with deposition of 100 nm Au on n-type Si substrates by a dc sputter deposition system (Helix) using a power of 50 W in argon partial pressure of 5 mTorr. A thin layer of Cr (~5 nm) was deposited on Si before the Au deposition to attain strong adhesion of Au on Si. Notably, the Au-interlayer was utilized to suppress the formation of

amorphous carbon (a-C), which usually formed prior to the nucleation of diamond in conventional microwave plasma enhanced chemical vapor deposition system (MPECVD) process.[57,58] The transport of electrons from the Si-substrate to diamond films will thus be enhanced due to Au interlayer. The Au coated Si samples were ultrasonicated for 45 min in methanol solution containing the mixture of diamond powder (about 4 nm in size) and Ti powder (SIGMA-Aldrich) (365 mesh) prior to the growth of diamond films. The three kinds of diamond films were grown on Au coated Si in a microwave plasma enhanced chemical vapor deposition (MPECVD) apparatus (IPLAS, Cyrannus) with different growth conditions. Ultrananocrystalline diamond (UNCD) films were grown by Ar(99%)/CH_4(1%) plasma with process pressure of 120 Torr and microwave power of 1200 W for 5 h with substrate temperature around 450^{o}C, whereas nitrogen incorporated UNCD (N-UNCD) films were grown by N_2(94%)/CH_4(6%) plasma with microwave power of 1200 W, process pressure of 50 Torr, substrate temperature of 700^{o}C and growth time of 1 h. In contrast, the hybrid granular structured diamond (HiD) films were grown by a two-step MPECVD process, in which we first grew 200 nm UNCD film for 1 h using above-mentioned growth conditions to serve as nucleation layer, followed by the deposition of diamond film using H_2 (50%)/Ar(49%)/CH_4 (1%) plasma at power 1300 W, process pressure of 80 Torr and growth time of 1 h. It should be mentioned that HiD films investigated in previous studies have observed that these films possess hybrid granular structure with enhanced EFE properties even better than the UNCD films.[59]

The morphology and microstructure of the diamond films were studied using field emission scanning electron microscopy (FESEM; JEOL 6500) and transmission electron microscopy (TEM; JEOL 2100 F), respectively. The bonding characteristics for all these films were examined using UV Raman (λ= 325 nm; Lab Raman HR800; Jobin Yvon, Inc., NJ, USA) and near edge X-ray absorption fine structure spectroscopy (NEXAFS, NSRRC, Taiwan). The EFE behavior of materials was measured by a parallel plate set-up, in which the anode was a Mo rod (2 mm in diameter) and the

cathode was the diamond films. The anode-to-cathode separation was controlled by a micrometer. The EFE current densities versus electrical field (J_{efe}−E) characteristics were attained using Keithley 2410 (USA) electrometer and these were explained using the Fowler-Nordheim (F-N) theory.[60]

To investigate the feasibility of using these diamond films as cathode for a microplasma device, which used an indium tin oxide (ITO)-coated glass as anode and the diamond films are cathode materials. The cathode-to-anode separation was fixed by a polytetrafluoroethylene (PTFE) spacer (1.0 mm in thickness) and a hole about 3.0 mm in diameter was cut out from the PTFE spacer to form a microcavity. The plasma was triggered using a direct current voltage source, which can reach up to the maximum applied voltage of 1000 V and was connected to device through a 500 kΩ resister . Prior to measurements, all samples were heated at 200^{o} C in vacuum for 1 h to remove moisture from surface of the films to attain reliable results. The chamber was evacuated to reach a base pressure of 0.1 mTorr and then purged with Ar for 10 min. The Ar gas was channeled into the chamber at a flow rate of 10 sccm and the PI measurements were carried out at pressure of 2 Torr. Plasma intensity of the microplasma devices were examined by an optical emission spectroscopy (OES; BWTEK, BWSpec 3.25, Newark, DE, USA) near an Ar emission line, i.e., in the region of near Infra-red (NIR, 811.5 nm), with the applied voltage of 430 to 550 V (voltage across the plasma).

Results and Discussion

A. Plasma illumination behavior of the microplasma devices based on diamond cathode materials

The main objective in the synthesis of diamond films is for the application as cathode materials in microplasma devices. The PI behavior of the microplasma devices was investigated first to understand how the different characteristics of these cathode materials influenced the devices performances. Figures 1a, 1b and 1c show the OES of NIR (812.5 nm) of the microplasma devices using UNCD, N-UNCD and HiD as cathodes, respectively, with the corresponding PI images shown

as insets. These results depict the increase in intensity of Ar plasma with the applied voltage, which is better illustrated by the voltage dependence of integrated intensity of 811.5 nm spectra line in Fig. 2a. This figure shows that the N-UNCD based microplasma devices perform better than those of other two devices by showing high intensity. Moreover, the variation of plasma current density, $(J_e)_{PI}$, against the applied voltage characteristics were shown in Fig. 2b, where the onset of plasma ignition, at 2 Torr is designated as the threshold breakdown voltage $(V_{th})_{PI}$. Curve I in Fig. 2b shows that the $(V_{th})_{PI}$= 433 V for UNCD based device and plasma current density $(J_e)_{PI}$ increased linearly with the applied voltage, reaching a $(J_e)_{PI}$ value of 3.49 mA/cm^2 at an applied voltage 623 V. Curve II in Fig. 2b depicts that, in case of N-UNCD based devices, the $(V_{th})_{PI}$= 399 V and the $(J_e)_{PI}$ values also increase linearly with applied voltage, reached $(J_e)_{PI}$ value of 3.98 mA/cm^2 at an applied voltage of 580 V, whereas curve III in Fig. 2b indicates that, for HiD based devices, the $(V_{th})_{PI}$= 415 V and the $(J_e)_{PI}$ value reached 3.67 mA/cm^2 at applied voltage of 615 V.

From each $(J_e)_{PI}$ -values, we can calculate the plasma density (n_e), by using Child's law shown as equation (1).[61]

$$n_e = \frac{J_c}{eu_B} \quad (1)$$

Here n_e is the electron density, J_c is plasma current density at cathode, e is the electron charge and u_B is the Bhom velocity. Bhom velocity of Ar ion is strictly depending on the kinetic energy of the electron and the mass of ion, which has described as below equation (2).[62]

$$u_B = \sqrt{\frac{kT_e}{m_i}} \quad (2)$$

here k is the Boltzmann constant, m_i is Ar ion mass and T_e is electron temperature is 7840 K.[63] Now submit the equation (2) in to (1) gives the equation for measurements of n_e, which shown as the equation (3).

$$n_e = \frac{J_c\sqrt{mi}}{e\sqrt{kT_e}} \quad (3)$$

Figure 2c shows the n_e-V characteristics of these devices, revealing that the n_e increased linearly with the applied voltage and reaching n_e value of $(n_e)_{UNCD}$ = 1.42 x 10^{17} /m^3 at an applied voltage 553 V for UNCD based device (curve I); $(n_e)_{N\text{-}UNCD}$ = 1.87 x 10^{17} /m^3 at an applied voltage of 550 V for N-UNCD based device (curve II) and $(n_e)_{HiD}$ = 1.54 x 10^{17} /m^3 at an applied voltage of 555 V for HiD based device (curve III). These plasma parameters were listed in Table 1. The PI behavior measurements clearly indicate that N-UNCD and HiD based devices perform better as compared to that of the UNCD-based ones, viz. they have the lower threshold voltage and can achieve higher plasma density. It is to be noted that the N-UNCD based devices are superior to that of the HiD based ones.

Generally, gas discharges in a device will be ignited by the impact of EFE electrons from cathode, photoionization, γ-ray irradiation (by radioactive elements present near by the device) and cosmic ionization,[61] whereas the sustaining of the plasma relies on the efficient supply of electrons from the cathodes for inducing cascade ionization of Ar-species in the plasma. Diamond films are known to possess high ion bombardment induced (Auger electrons) γ-coefficient.[62] However, the γ-coefficient of diamond films is insignificantly different for the diamond films with different morphology and phase constituents.[49] There must be other source of electrons for sustaining the plasma, which make the N-UNCD and the HiD based devices performing overwhelmingly better than that of the UNCD based ones. The field emitted electrons are the possible source, as previous

studies observed that the high EFE materials do lead to large plasma current density.[63] To investigate the possible contribution of the field emitted electrons to the plasma process, we have measured the EFE current density versus applied field (J_{efe}–E) characteristics, which were modeled by the F-N theory.[60]

$$J_{efe} = \left(\frac{A\beta^2 E^2}{\phi}\right)\exp\left(\frac{-B\phi^{\frac{3}{2}}}{\beta E}\right) \quad (4)$$

Where $A = 1.54 \times 10^{-6}$ A eV V^{-2} and $B = 6.83 \times 10^{9}$ $eV^{-3/2}$ V m^{-1}, β is the field-enhancement factor, E is the applied field and φ is the work function of the emitting materials (5.2 eV for diamond). The turn-on field (E_0) for EFE process was designated as the intercepts of the straight lines extrapolated from the high-field and the low-field segments of the F-N plots. The J_{efe} -E curves of UNCD, N-UNCD and HiD films are shown in the Fig. 3, with the inset revealing the F-N plots. This figure shows that the EFE process for UNCD films can be turned on at $(E_0)_{UNCD}$= 7.96 V/μm, achieving an EFE current density of $(J_{efe})_{UNCD}$ = 4.26 mA/cm^2 at an applied field of 15.5 V/μm (curve I). In case of the N-UNCD films, the EFE process can be turned on at $(E_0)_{N\text{-}UNCD}$= 2.07 V/μm with large EFE current density of $(J_{efe})_{N\text{-}UNCD}$ = 5.42 mA/cm^2 at an applied field of 4 V/μm (curve II). In contrast, for HiD films, the EFE process can be turned on at $(E_0)_{HiD}$= 4.5 V/μm with EFE current density of $(J_{efe})_{HiD}$ = 4.75 mA/cm^2 at an applied field of 9.2 V/μm (curve III). These EFE parameters were also listed in Table 1 to facilitate the comparison. The N-UNCD and HiD films exhibited overwhelmingly superior EFE properties to the UNCD films which could be the key parameter, resulting in better PI performance for the N-UNCD and the HiD based microplasma devices as compared with the UNCD based ones.

Actually, in practical application, the optimization of lifetime is a crucial parameter of concern for any microplasma device. Lifetime of these devices was evaluated in Ar gas atmosphere at

working pressure of 50 Torr with applied DC power of 0.5 W (designated as J_{e1} profile) or 1 W (designated as J_{e2} profile). The lifetime measurements in Ar plasma for UNCD, N-UNCD and HiD based devices were shown in Fig. 4. For the case of UNCD based devices, the J_{e1} profile started to decay at 2.09 days (curve I, Fig. 4a) and onset of J_{e2} profile decaying decreased to 21.7 h for applied power of 1 W (curve II, Fig. 4a). In contrast, for the N-UNCD based device, J_{e1} profile started to decay in 2.02 days (curve I, Fig. 4b), whereas J_{e2} profile started to decay at 20 h (curve II, Fig. 4b). In case of the HiD based device, J_{e1} profile started to decay in 4.0 days (curve I, Fig. 4c), whereas J_{e2} started to decay at 24.5 h (curve II, Fig. 4c). Interestingly the HiD based devices show longest lifetime compared with those of UNCD and N-UNCD based devices.

B. Materials characteristics of the diamond cathode materials used in microplasma devices

These lifetime measurements clearly indicated that the microplasma devices based on N-UNCD films cannot last as long as UNCD films, although the N-UNCD films possess overwhelmingly superior EFE properties and PI performances than that of the UNCD films. The N-UNCD films are thus not ideal cathode materials for microplasma devices. In contrast, not only the HiD films possess superior EFE properties to the UNCD films, but also the HiD based microplasma devices exhibit better PI performance and are more robust than the UNCD based ones. The HiD films seem to be better choice for serving as cathode materials for the microplasma devices. To investigate the genuine mechanism that influenced the EFE, PI and robustness of the microplasma devices, the characteristics of these diamond cathode materials were studied thoroughly.

Figure 5 shows the FESEM images of diamond cathode materials grown on the Au coated Si. The surface morphology of Ar plasma grown UNCD films is very smooth (Fig. 5a), which is due to the ultra-small diamond grains of size (around 5−10 nm) contained in these films. Whereas the surface morphology of N_2 plasma grown N-UNCD films contain the horizontally spread elongated

wire-like structures (Fig. 5b) and the surface morphology of 2-step MPECVD grown HiD films appears cauliflower-like morphology with large equi-axed grains of size 40–50 nm (Fig. 5c). These granular structures of UNCD, N-UNCD and HiD films are exactly the same as those grown directly on bare Si-substrates. Although the utilization of Au interlayer will markedly enhance the EFE behavior of the films.[57,58] it does not much affect the surface morphologies of UNCD and N-UNCD films.

The bonding structure of the diamond films were shown by the UV Raman spectroscopy in Fig. 6. Figure 6a reveals that, the UNCD films contain diffuse Raman resonance peaks, which can be deconvoluted into ν_1 at 1172 cm^{-1}, D-band at 1336 cm^{-1}, D*-band at 1367 cm^{-1}, and G-band at 1580 cm^{-1}. The ν_1 mode indicates the presence of *trans*-polyacetylene (*t*-PA) along the grain boundaries of UNCD films grown on Si.[64] The D-band corresponds to the diamond materials, whereas the D*-band and G-band imply the presence of disordered carbon and ordered graphitic phase, respectively.[65, 66] The relatively smaller D-band resonance peaks compared with the G-band and similar intense D*-band implies that the UNCD films are predominated with sp^2-bonded carbons. To obtain the clearer depiction on bond structures of carbon in diamond, we have measured NEXAFS. The curve I in Fig. 7 indicates that, for UNCD films, there appears an abrupt rise at 289.84 eV, corresponding to electron core excitation of C-C (1 s)-σ* band, and a second absorption valley at 301.06 eV. These are the signature of diamond.[67-69] Very small signal of C1s-π* band at 283.7 eV was observable. The NEXAFS reveals clearly that the UNCD films are predominated with sp^3-bonded carbon, the diamond.

In case of N-UNCD film grown on Au coated Si, UV Raman spectrum (Fig. 6(b)) also shows the presence of ν_1- (1168 cm^{-1}), D- (1338 cm^{-1}), D*- (1392 cm^{-1}), and G- (1598 cm^{-1}) bands. The intensity of D*-band is much higher than D band, implying the presence of large amounts of disorder carbon in N-UNCD films. Again, the NEXAFS spectrum for N-UNCD films was examined to elucidate the nature of bonding in these films. Curve II in Fig. 7 shows that the N-UNCD films were

also predominated with C1s-σ* band and a second absorption valley, but with a large C1s-π* observed at 283.7 eV. These observations imply that the N-UNCD films are diamond, but contain larger proportion of sp^2-bonded carbon.[70,71] In contrast, the Raman spectrum of HiD film, which was shown in the Fig. 6c, revealing the presence of sharp and high intensity of D-(1338 cm^{-1}), besides the broaden ν_1-(1170 cm^{-1}) and G-(1580 cm^{-1}) bands. The presence of high intensity D-band simultaneously with the other diffuse Raman peaks is an indication of the presence of large diamond and ultra-small grains at the same time in HiD films.[65,66] NEXAFS results of the HiD films shown as curve III in the Fig. 7 is also similar to those of the UNCD films, viz. the spectrum contains C-C (1s)-σ* at 289.84 eV and second absorption valley at 301.06 eV that are the signature of sp^3-bonded carbon, the diamond.[67-70] The C1s-π* was observed at 283.7 eV but the peak intensity is not as large as that in N-UNCD film, indicating the presence of some graphitic phase in the HiD films[69,70] but the amount of graphitic phase is much less than those of N-UNCD films.

The above-described studies are not sufficient for understanding the different behavior in serving as cathode materials of microplasma devices. For this purpose, the TEM microstructure of these films was examined. The bright field (BF) TEM micrograph shown in Fig. 8a reveals that the UNCD films contain uniformly nanosized grains with a few aggregates of diamond grains sparsely distributed over the samples. Notably, these aggregates are soft agglomerates, as they can be disintegrated easily due to the electron irradiation during the TEM investigation. The inset in Fig. 8a reveals that the selective area electron diffraction (SAED) pattern contains mainly the ring shaped patterns corresponding to the (311), (220), and (111) lattice-planes of diamond, indicating that the materials are diamond with randomly oriented nanosized diamond grains. There exists a prominent diffused ring in the center of this SAED, indicating the existence of some graphitic (or a-C) phase in these films. The size distribution of the diamond grains in these films are better illustrated by the composed dark field (c-DF) images, which are the superposition of several dark field images, acquired using different diffraction spots. Figure 8b shows the c-DF images of UNCD films

corresponding to the BF image in Fig. 8a, which were superposition of DF images taken from three different diffraction spots (blue, red and green color circles in the inset SAED pattern of Fig. 8b), indicating that the films contain many ultra-small diamond grains of sizes about 5–10 nm and the some diamond aggregates scarcely distributed among the ultra-small grain matrix.

More detailed investigations were carried out for the identification of different phase constituents in UNCD/Au-Si films by high resolution TEM (HRTEM) studies. Figure 8c shows the structure image for UNCD films corresponding to the region designated by arrow in Fig. 8a, indicating that this material consists of both the regions with straight lattice fringes corresponding to diamond aggregates (lower left corner) and some nano-sized diamond grains (indicated by arrows in Fig. 8c) dispersed in the regions with curved fringes. The region with curved fringes corresponds to graphitic phase (center and upper right corner). The Fourier transformed (FT) image of the whole structure image (FT_0) shows a spotted diffraction pattern arranged in a ring, which is of diamond (d) phase, and donut-shaped diffused diffraction ring located at the center of the FT image, which corresponds to graphitic (g) phase. The presence of diamond materials is highlighted by the FT image, FT_1, corresponding to the region "1", whereas the presence of nano-graphitic phase is highlighted by the FT image, FT_2, corresponding to the region "2".

Electron energy loss spectroscopy (EELS) spectra were recorded in the carbon K-edge region to unambiguously distinguish between the different carbon materials such as diamond, graphite and a-C.[72] Curve I of Fig. 9a and 9b show, respectively, the selected area core-loss and plasmon-loss EELS spectra corresponding to the BF images of Figs. 8a. Cure I in Fig. 9a shows that the core-loss EELS spectra of UNCD films are similar with the corresponding NEXAFS (cf. curve I, Fig. 7). The carbon edge core-loss EELS spectra of UNCD films indicate the presence of abrupt rise near 290.5 eV (σ*-band) and a large dip in the vicinity of 302 eV, inferring the diamond nature of these materials.[73,74] Moreover, there is a small π*-band at 285.5 eV in this core-loss EELS spectra, inferring the presence of some sp^2-bonded carbons in UNCD films. However, it is still necessary to

differentiate the nature of the sp^2-bonded carbon to understand the genuine mechanism, which alters the characteristics of these diamond films. It should be pointed out that the plasmon-loss EELS spectra is the most effective measurement for distinguishing the crystalline sp^2-bonded carbon (the graphite) from the amorphous ones, as the plasmon-loss EELS spectra for the graphitic phase shows a prominent peak at s_3 (27 eV) and those for the *a-C* phase shows a peak at s_1 (22 eV).[74,75] In contrast, the crystalline sp^3-bonded carbons, the diamond, shows a peak consequent to the bulk plasmon at s_4 (33 eV) with a shoulder corresponding to the surface plasmon at s_2 (23 eV). The I_{s2}/I_{s4} ratio is about $1:\sqrt{2}$.[74,75] Curve I in Fig. 9b shows the plasmon-loss EELS spectra of the same regions of UCND films in Fig. 8a, revealing that the UNCD films are dominated with s_2 and s_4 peaks, indicating that UNCD films are predominantly diamond.[74,75]

In contrast, Fig. 10a depicts a BF-TEM image of the N-UNCD film grown using N_2/CH_4 plasma with clear evidence of the formation of needle-like diamond grains of a length of 50–400 nm and a few nanometers in diameter. The SAED contains, besides the sharp diffraction rings corresponding to the (311), (220), and (111) lattice-planes of diamond, a more prominent diffused ring in the center compared with those of UNCD films (cf. Fig. 8a), signifying the existence of larger proportion of graphitic phase in these films. Figure 10b evinced the c-DF image of the films corresponding to the BF image in Fig. 10a, indicating clearly the growth of diamond as needle-like structures. Furthermore, the detail granular structure of the N-UNCD is unraveled by the HRTEM micrograph (Fig. 10c), exhibiting a clear core-shell microstructure. Each wire-like grain is encased by a few graphite layers with the thickness up to around 5 nm. The FT_0 image shown in the inset of Fig. 10c illustrates a bright spotted diffraction spot corresponding to needle-like diamond grains and weaker diffraction patterns arranged in a ring, which corresponds to randomly oriented diamond (d) grains. Moreover, there is a donut shaped diffused diffraction ring located at the center of the FT image, which corresponds to graphitic (g) phase lying in the matrix of the materials. The diamond and graphitic structures are further confirmed by FT diffractograms corresponding to the selected

areas. The FT_1 pattern from the marked area "1" gives the diamond structure, whereas the FT_2 pattern from the marked area "2" points to the graphitic structure. These results confirm that each needle-like nanowire is diamond, which is encapsulated by a sheath of graphitic phase.

Curve II in Fig. 9a shows that the core-loss EELS spectra of N-UNCD films are similar with those of UNCD films (cf. curve I, Fig. 9a), i.e., containing an abrupt rise near 290.5 eV (σ*-band) and a large dip in the vicinity of 302 eV that inferred the diamond nature of these materials.[73,74] Moreover, there is a more prominent π*-band at 285.5 eV in the core-loss EELS spectra of N-UNCD films compared with those of UNCD films, inferring the presence of more abundant sp^2-bonded carbons in N-UNCD films. The plasmon-loss EELS spectrum of N-UNCD films (curve II, Fig. 10b) is dominated by larger s_3-band (~27 eV) with the s_2 and s_4-bands of much smaller intensity, indicating that this region consists of larger proportion of graphitic phases than diamond.

These TEM microstructures indicate that the prime factor by which the N-UNCD films possess overwhelmingly superior EFE properties to the UNCD films is the presence of graphitic sheath along the needle-like diamond grains. This graphitic sheath with good crystallinity conducts better the electrons compared with the a-C phase contained in the grain boundaries of the UNCD films. However, the graphite sheath is not as strong as the sp^3-bonded diamond that rendered the N-UNCD films more susceptible to the Ar-ion bombardment erosion. Therefore, the microplasma devices utilizing the N-UNCD films as cathode cannot last as long as those used UNCD films as cathode. These observations imply that the possible way of enhancing the PI performance of the microplasma devices without sacrificing their robustness is to develop materials with proper microstructure.

Interestingly, the HiD based microplasma devices not only possess superior PI performance but also exhibit better robustness, compared with those based on UNCD films. Such a behavior is different from those of N-UNCD based microplasma devices, which own superior PI properties but with inferior lifetime stability. To understand how the HiD films possess superior EFE properties, yet the corresponding microplasma devices still show better robustness compared with the UNCD ones,

the microstructure and the bonding structure of the HiD films was also investigated, respectively, using TEM and EELS. Figure 11a shows the BF-TEM micrograph of HiD films, which reveals that the films contain large diamond aggregates, about a few hundred nanometers in size, dispersed evenly among the ultra-small grain matrix, forming a hybrid granular structure. The c-DF image of HiD films in Fig. 11b corresponding to the BF image in Fig. 11a shows more clearly the existence of large diamond aggregates (blue and green regions) of dimensions around 30–80 nm among the ultra-small diamond grains (red regions). The SAED shown as inset in Fig. 11a contains spotty diffraction spots arranged in a ring geometry, corresponding to (111), (220), and (311) lattices of diamond, which is owing to the co-existence of the large diamond aggregates and the randomly oriented nano-sized diamond grains in the film. The detail microstructures of the HiD films were further examined using HRTEM. The FT_0 (inset, Fig. 11c) shows the presence of streaks associated with the major diffraction spots, which corresponds to the planar defects, the stacking faults, contained in the large diamond aggregates that is highlighted by FT_1 image corresponding to the marked area "1" in Fig. 11c. The presence of planar defects implied that the large aggregates were formed by the coalescence of the ultra-small diamond grains.[76] Moreover, there exists a diffused diffraction ring located at the center of the FT_0 image, which corresponds to graphitic (or a-C) phase, indicating that the regions adjacent the large diamond aggregates contain large proportion of sp^2-bonded carbon, which is highlighted by the FT_2 image corresponding to the marked area "2". The proportion of sp^2-bonded carbon in HiD films is much less than that in N-UNCD films.

Curve III of Fig. 9a shows the carbon edge core-loss EELS spectra of the HiD films, indicating the presence of abrupt rise near 289.5 eV (σ*-band) and a large dip in the vicinity of 302 eV, that is similar with those of UNCD and N-UNCD films, inferring the diamond nature of these materials.[73,74] No π*-band at 285.5 eV was observable, indicating less sp^2-bonded carbon contained in HiD film. The plasmon-loss spectrum for HiD films (curve III, Fig. 9b) is subjugated by s_3-band (27 eV), but the s_2- and s_4-bands still dominate. These observations indicate that the HiD films contain less

sp^2-bonded carbon than the N-UNCD films (but more graphitic phase than the UNCD films). These EELS results imply that although the region "2" in Fig. 11c shows abundant curved fringes and no parallel fringes representing diamond lattice planes was observable; this region is still predominately diamond. The lattice fringes are not observable simply because that the diamond grains in this region was oriented away from a zone axis, weakly diffracting the electrons and showing no phase contrast. The curved fringes corresponding to nanographite phase are thus showing up. The nanographite phase is located above (or beneath) the diamond grains. Restated, Fig. 11c shows that the HiD films have graphitic phase embedded in the boundaries between the large diamond aggregates and the matrix of ultra-small diamond grains that can still enhance the electron transport, but will not be easily eroded by the bombarding Ar-ions. Therefore, utilization of HiD films as cathode materials can enhance the plasma illumination behavior, but will not degrade the lifetime stability for the microplasma devices.

CONCLUSIONS

Parallel-plate kind of microplasma devices have been made by using diamond films as cathode materials. Raman spectroscopy, NEXAFS and TEM studies reveal that, for N-UNCD films, formation of more graphite phases around the diamond grains resulted in enhanced EFE properties for the films. As a result, microplasma device based on these films shows better PI properties due to enhanced EFE properties. But the lifetime studies in Ar plasma show the material erosion within a few days for applied power of 0.5 W for N-UNCD based devices due to the inevitable exposure of graphitic phases, which encased the needle-like diamond grains, to the Ar plasma. To achieve good EFE properties as well as longer lifetime, we have developed HiD films, which contain sp^2-bonded carbons embedded in the boundaries of diamond grains. Such HiD films not only exhibit excellent EFE properties and thus better PI performance, but also show better robustness for the corresponding microplasma devices, viz. longer lifetime of four days for an applied DC power of 0.5 W in Ar plasma. From all above studies, we conclude that the HiD films grown on Au coated Si can be

applied as the electrodes for microplasma devices. This investigation sheds a light on the development of next generation cathode materials for microplasma devices due to its enhanced PI properties and longer lifetimes.

ACKNOWLEDGEMENTS

The authors would like to thank the National Science Council, Republic of China, for the support of this research through the project No. NSC 101-2112-M-032-002.

The authors declare no competing financial interest.

Notes and References

[a]Department of Engineering and System Science, National Tsing Hua University, Hsinchu 300, Taiwan, R.O.C.; *E-mail: kcleou@ess.nthu.edu.tw

[b]Department of Materials Science and Engineering, National Tsing Hua University, Hsinchu 300, Taiwan, R.O.C.;

[c]Scientific Research Division, National Synchrotron Radiation Research Center, Hsinchu 300, Taiwan, R. O. C.;

[d]Department of Physics, Tamkang University, Tamsui 251, Taiwan, R.O.C. *E-mail: inanlin@mail.tku.edu.tw

1 M. Kogoma and S. Okazaki, *J. Phys. D: Appl. Phys,* 1994, **27**, 1985–1987.

2 R. Dorai and M.J. Kushner, *J. Phys. D: Appl. Phys.* 2003, **36**, 666–685.

3 W.S Kang, J.M. Park, Y. Kim, and S.H Hong, *IEEE Trans. Plasma Sci*. 2003, **31**, 504–510.

4 D. Braun, V. Gibalov, and G. Pietsch, *Plasma Sources Sci. Technol*. 1992, **1**, 166–174.

5 V. Gibalov and G.J. Pietsch, *J. Phys. D: Appl. Phys.* 2000, **33**, 2618–2636.

6 V.I Gibalov and G.J Pietsch, *J. Phys. D: Appl. Phys.* 2004, **37**, 2082–2092.

7 T. Callegari, R. Ganter and J.P Boeuf, *J. Appl. Phys*. 2000, **88**, 3905–3913.

8 K. Zhang, B. Eliasson and U. Kogelschatz, *Ind. Eng. Chem. Res*. 2002, **41**, 1462–1468.

9 T. Hammer, *Contrib. Plasma Phys*. 1999, **39**, 441–462.

10 M.W Manheimer, L.E Sugiyama and T.H Stix, (ed) Plasma Science and The Environment (Woodbury, NY: American Institute of Physics) 1997.

11 M. Laroussi, I. Alexeff and W.L Kang, *IEEE Trans.Plasma* Sci. 1998, **28**, 184–188.

12 M. Laroussi, *IEEE Trans. Plasma Sci*. 1996, **24**, 1188–1191.

13 M. Laroussi, G.S. Sayler, B.B. Glascock, B. McCurdy, M.E. Pearce, N.G. Bright and C.M Malott, *IEEE Trans. Plasma Sci.* 1999, **27**, 34–35.

14 E. Stoffels, A.J. Flikweert, W.W. Stoffels and G.M.W. Kroesen, *Plasma Sources Sci. Technol.* 2002, **11**, 383–388.

15 D. Mariotti and R.M. Sankaran, J. Phys D: Appl Phys 2010, **43**, 323001.

16 R.M. Sankaran, D. Holunga, R.C. Flagan, and K.P. Giapis, Nano. Lett. 2005, **5**, 537–541.

17 H.C. Thejaswini, A.R. Hoskinsona, B. Agasanapura, M. Grunde, J. Hopwood, *Diamond Relat. Mater,* 2014, **48**, 24–31.

18 E. J. Szili, S. A. Al-Bataineh, P. Ruschitzka, G. Desmet, C. Priest,b H. J. Griesser, N. H. Voelcker, F. J. Harding, D. A. Steelea and R. D. Short, *RSC Advances*, 2012, **2**, 12007–12010.

19 S. Fan, Y. T. Shen, L.P. Tsai, C.C. Hsu, F.H. Ko, and Y.T. Cheng, *Lab Chip*, 2012, **12**, 3694–3699.

20 G. Desmet, A. Michelmore, E.J. Szili, S.J. Park, J. G. Eden, R. D. Shorta and S.A. Al-bataineh, *RSC Adv*., 2013, **3**, 13437–13445.

21 M.J. Kushner, *J. Phys. D: Appl. Phys*. 2005, **38**, 1633–43.

22 J.P. Boeuf, L.C. Pitchford and K.H. Schoenbach, *Appl. Phys. Lett.* 2005, **86**, 071501.

23 J.H. Seo, and J.G. Eden, *J. Appl. Phys.* 2006, **100**, 123302.

24 K.H. Schoenbach, M. Moselhy, W. Shi and R. Bentley, *J. Vac.Sci. Technol.* A 2003**, 21**, 1260–1265.

25 P. Kurunczi, H. Shah and K. Becker, *J. Phys. B: At. Mol. Opt.Phys.* 1999, **32**, L651.

26 I. Petzenhauser, L.D. Biborosch, U. Ernst, K. Frank and K.H. Schoenbach, *Appl. Phys. Lett.* 2003***, 83***, 4297.

27 von, A.P.; Sadler, D. J.; Jensen, C.; Ostrom, N. P.; McCain, S. T.; Vojak, B. A.; Eden and J. G. Linear, *Appl. Phys. Lett.* 2003, **82,** 4447–4449.

28 A.P. Von, S.T. McCain, N.P. Ostrom, B.A. Vojak, J.G. Eden, F. Zenhausern, C. Jensen and M. Oliver, *Appl. Phys. Lett.* 2003, **82***, 2562*–2564.

29 S.J. Park Eden and J. G. *Electron. Lett.* 2003, **39**, 773–775.

30 J.W. Frame, D.J. Wheeler, T.A. DeTemple and J.G. Eden, *Appl. Phys. Lett.* 1997, **71**, 1165.

31 J. Chen, S.J. Park, Z. Fan, J.G. Eden, C. Liu, *J. Microelectromech. Syst.* 2002, **11**, 536–542.

32 J.W. Frame and J.G. Eden, *Electron. Lett.*1998, **34**, 1529–1531.

33 S.J. Park, C.J. Wagner and J.G. Eden, *IEEE Photon. Technol. Lett.*2001, **13**, 61–63.

34 S.J. Park, J. Chen, C. Liu and J.G.Eden, *Appl. Phys. Lett.* 2001, **78**, 419–421.

35 S.J. Park, J. Chen, C. Liu, and J.G. Eden, *Electron. Lett.* 2001, **37**, 171–172.

36 S.J. Park, J.G. Eden, J. Chen, C. Liu, *Appl. Phys. Lett.* 2001, **79**, 2100–2102.

37 S.J. Park, J.G. Eden, J. Chen, C. Liu, J. Ewing, J. *Opt. Lett.* 2001, **26,** 1773–1775.

38 R. Block, O. Toedter, K.H. Schoenbach, Proc. 30th AIAA Plasma Dynamics and Lasers Conf. (Norfolk, VA,*)* 1999**,** 3434.

39 R. Block, M. Laroussi, F. Leipold, K.H. Schoenbach, Proc. 14th Int. Symp. on Plasma Chemistry (Prague, Czech Republic) 1999*,* 945.

40 L. Aguilera, I. Montero, M.E. D´avila, A. Ruiz1, L. Gal´an, V. Nistor, D. Raboso, J. Palomares, F. Soria, *J. Phys. D: Appl. Phys.* 2013, **46**, 165104.

41 J.E. Field, Ed. The Properties of Diamond; Academic Press: London, 1979, 4−22.

42 C.E. Nebel, B. Rezek, D. Shin, H. Uetsuka, N. Yang, *J. Phys. D: Appl. Phys*. 2007, **40**, 6443–6466.

43 M.G. Dieter, *Annu. Rev. Mater. Sci.*1999, **29,** 211–259.

44 W. Zhu, C. Bower, G.P. Kochanski and S. Jin, *Solid- State Electrochem*. 2001, **45,** 921–928.

45 L.S. Pan, D.R. Kania, Diamond: Electronic Properties and Applications (Klumer Academic, Boston, 1995).

46 P.K. Bachmann, E.V. Van, D.U. Wiechert, G. Zhong, J. Robertson, *Diam. Relat. Mater.* 2001, **10**, 809–817.

47 H.C. Chen, S.C. Lou, C.L. Chen, R.H. Tang, W.C. Shih, S.C. Lo, L.J. Lin, C.Y. Lee, I.N. Lin, *J. Vac. Sci. Technol. B* 2013, **31(2)**, 02B109.

48 S.C. Lou, C.L. Chen, K.Y. Teng, C.Y. Tang and I.N. Lin, *J. Vac. Sci. Technol. B* 2013, **31(2)**, 02B109.

49 K.J. Sankaran, K. Srinivas, H.C. Chen, C.L. Dong, K.C. Leou, C.Y. Lee, N.H. Tai andI.N. Lin *J. Appl. Phys.* 2013, **114**, 054304.

50 S. Mitea, M. Zeleznik, M. D. Bowden, P.W. May, N.A. Fox, J. N. Hart, C. Fowler, R. Stevens and N. StJ. Braithwaite, *Plasma Sources Sci. Technol*. 2012, **21**, 022001.

51 T.H. Chang, K. Srinivasu, Y.J. Hong, K.C. Leou, T.R. Yew, N.H. Tai, and I.N Lin, ACS *Appl. Mater. Interfaces* 2014, 6, 11589−11597.

52 T.H. Chang, K. Srinivasu, K.J. Sankaran, K.C. Leou, T.R. Yew, N.H. Tai, and I.N Lin, *Appl. Phys. Lett.* 2014, **104**, 223106.

53 T.H Chang, S.C. Lou, H.C. Chen, C.L. Chen, C.Y. Lee, N.H Tai and I.N Lin, *Nanoscale*, 2013, **5**, 7467–7475.

54 A. R. Krauss, D. M. Gruen, D. Zhou, T. G. McCauley, L. C. Qin, T. D. Corrigan, O. Auciello, and R. P. H. Chang, Mater. Res. Soc. Symp. Proc. **495**, 299 (1998).

55 K. J. Sankaran, J. Kurian, H.C. Chen, C.L. Dong, C.Y. Lee, N.H.Tai and I.N. Lin, *J. Phys. D: Appl. Phys.* 2012, **45**, 365303.

56 H.F. Cheng, H. Y. Chiang, C. C. Horng, H. C. Chen, S. C. Wang and I. N. Lin, *J. Appl. Phys.* 2011, **109**, 033711.

57 K.J. Sankaran, K. J. K. Panda, B. Sundaravel, C.H. Chen, I.N. Lin, I. N, C.Y. Lee and N.H. Tai, *ACS Appl. Mater. Interfaces* 2012, **4**, 4169−4176.

58 Chen, H. C.; Sankaran, K. J.; Lo, S. C.; Lin, L. J.; Tai, N. H.; Lee, C. Y.; Lin, I. N. *J. Appl. Phys.* 2012, **112**, No. 103711.

59 R.H. Fowler, L. Nordheim, *Proc. R. Soc. London, Ser. A* 1928, **119**, 173-181.

60 M.A. Lieberman and A.J. Lichtenberg A J, Principles of plasma discharges and materials processing, 2nd Ed; John Wiley & Sons:Hoboken, NJ, 2005.

61 B. Chapman B, sputtering and plasma etching, John Wiley & Sons, New York, 1980.

62 K. Srinivasu, K.J. Sankaran, K.C. Leou, N.H. Tai and I.N. Lin, *Plasma Sources Sci. Technol.* 2014 (Submitted).

63 A.C. Ferrari and J. Robertson, *Phys. Rev. B* 2001, **63**, 121405.

64 T.D. Corrigan, D.M. Gruen, A.R. Krauss, P. Zapol, R.P. H. Chang, *Diamond Relat. Mater.* 2002, **11**, 43−48.

65 A.C. Ferrari and J. Robertson, *Phys. Rev. B* 2000, **61**, 14095.

66 J. Birrell, J.E. Gerbi, O. Auciello, J.M. Gibson, D.M. Gruen, J.A. Carlisle, *J. Appl. Phys.* 2003, **93**, 5606.

67 Y.K. Chang, H.H. Hsieh, W.F. Pong, M.H. Tsai, F.Z. Chien, P.K. Tseng, L.C. Chen, T.Y.Wang, K.H. Chen, J.R. Bhusari, J. R. Yang and S.T. Lin, S. T. *Phys. Rev. Lett*. 1999, **82**, 5377.

68 P.T. Joseph, N.H. Tai, C.H. Chen, H. Niu, H.F. Cheng, W.F. Pong and I.N. Lin, *J. Phys. D: Appl. Phys.* 2009, **42**, 105403.

69 J. Nithianandam, J.C Rife and H. Windischmann, *Appl. Phys. Lett.* 1992, **60**, 135.

70 A. Gutierrez, M.F. Lopez, I. Garcia and A. Vazquez, *J. Vac. Sci. Technol. A* 1997, **15**, 294.

71 A. Dato, V. Radmilovic, Z. Lee, J. Philips and M. Frenklach, *Nano. Lett.* 2008, **8**, 2012–2016.

72 D.M. Gruen, S. Liu, A.R. Krauss, J. Luo and X.Pan, *Appl. Phys. Lett*. 1994, **64**, 1502.

73 P. Kovarik, E.B.D. Bourdon and R.H. Prince, *Phys. Rev. B* 1993, **48**, 12123.

74 S. Prawer, J.L. Peng, J.O. Orwa, J.C. McCallum, D.N. Jamieson and L.A. Bursill, *Phys. Rev. B* 2000, **62**, R16360.

75 I.N. Lin, H.C. Chen, S.C. Wang, Y.R. Lee and C.Y. Lee, *CrystEngComm.* 2011, **13**, 6082–6089.

Table 1. The Plasma illumination and the electron field emission parameters of three kinds of diamond films.

Samples	Plasma illumination properties			Electron field emission properties	
	V_{th} (V)	n_e (/m^3)	τ (days)	E_0 (V/μm)	J_e (mA/cm^2)
UNCD	433	1.42 x10^{17} @ 553 V	2.09	7.96	4.26 @ 15.5 V/μm
N-UNCD	415	1.87 x10^{17} @ 550 V	2.02	2.07	5.42 @ 4.0 V/μm
HiD	390	1.54 x10^{17} @ 555 V	4.0	4.50	4.75 @ 9.2 V/μm

$(V_{th})_{PI}$: Threshold breakdown voltage of Ar gas.

n_e : Plasma density measured at an applied field of 5800 V/cm.

E_o: Turn-on field in EFE process.

J_{efe}: EFE current density measured at designated applied field.

τ: lifetime of a microplasma device measured at applied power of 0.5 W.

Figure captions

Figure 1. OES of Ar NIR line (811.5 nm) of the microplasma devices, which used (a) UNCD/Au-Si films (b) N-UNCD/Au-Si films and (c) HiD/Au-Si films as cathode. The insets show the corresponding PI images.

Figure 2. The voltage dependency of (a) Ar NIR (811.5 nm) spectral line intensiry, (b) The plasma current density versus applied, $(J_e)_{PI}$-E, characteristics and (c) the plasma density versus applied field, $(n_e)_{PI}$-E, characteristics of the microplasma devices, which used (I) UNCD/Au-Si film, (II) N-UNCD/Au-Si film and (III) HiD/Au-Si films as cathode.

Figure 3. The EFE characteristics, J_{efe}–E properties, of (I) UNCD/Au-Si films, (II) N-UNCD/Au-Si films and (III) HiD/Au-Si films. The inset shows the F-N plots of the UNCD/Au-Si films (curve I), N-UNCD/Au-Si films (curve II) and HiD/Au-Si films (curve III) [Error bars in the curves depicts the 4-6 % error in experimental data].

Figure 4. The lifetime measurements in Ar plasma environment with applied DC power of (I) 0.5 and (II) 1 W for the microplasma devices, which used (a) UNCD/Au-Si films, (b) N-UNCD/Au-Si films and (c) HiD/Au-Si films as cathode.

Figure 5. The SEM micrographs of (a) UNCD/Au-Si films, (b) N-UNCD/Au-Si films and (c) HiD/Au-Si films.

Figure 6. The UV-Raman spectra for (a) UNCD/Au-Si films, (b) N-UNCD/Au-Si films and (c) HiD/Au-Si films.

Figure 7. The NEXAFS spectra of (I) UNCD/Au-Si films, (II) N-UNCD/Au-Si films and (III) HiD/Au-Si films.

Figure 8. The (a) bright field and (b) composed dark field TEM micrographs of the UNCD/Au-Si films with the inset showing the corresponding SAED. (c) The TEM structure image of the region designated in “a”, where the ultra-small diamond grains were designated by arrows. The FT_0 represents the Fourier transformed (FT) diffractogram corresponding to the whole structure image. FT_1 and FT_2 represent the FT image of regions “1” and “2”, respectively.

Figure 9. The selected area (a) core-loss and (b) plasmon-loss EELS spectra for (I) UNCD/Au-Si films, (II) N-UNCD/Au-Si films and (III) HiD/Au-Si films.

Figure 10. The (a) bright field and (b) composed dark field TEM micrographs of the N-UNCD/Au-Si films with the inset showing the corresponding SAED. (c) The TEM structure image of the region designated in "A", where the FT_0 represents the Fourier transformed diffractogram corresponding to the whole structure image. FT_1 and FT_2 represent the FT images of regions "1" and "2", respectively.

Figure 11. The (a) bright field and (b) composed dark field TEM micrographs of the HiD/Au-Si films with the inset showing the corresponding SAED. (c) The TEM structure image of the region designated in "a", where the FT_0 represents the Fourier transformed diffractogram corresponding to the whole structure image. FT_1 and FT_2 represent the FT images of regions "1" and "2", respectively.

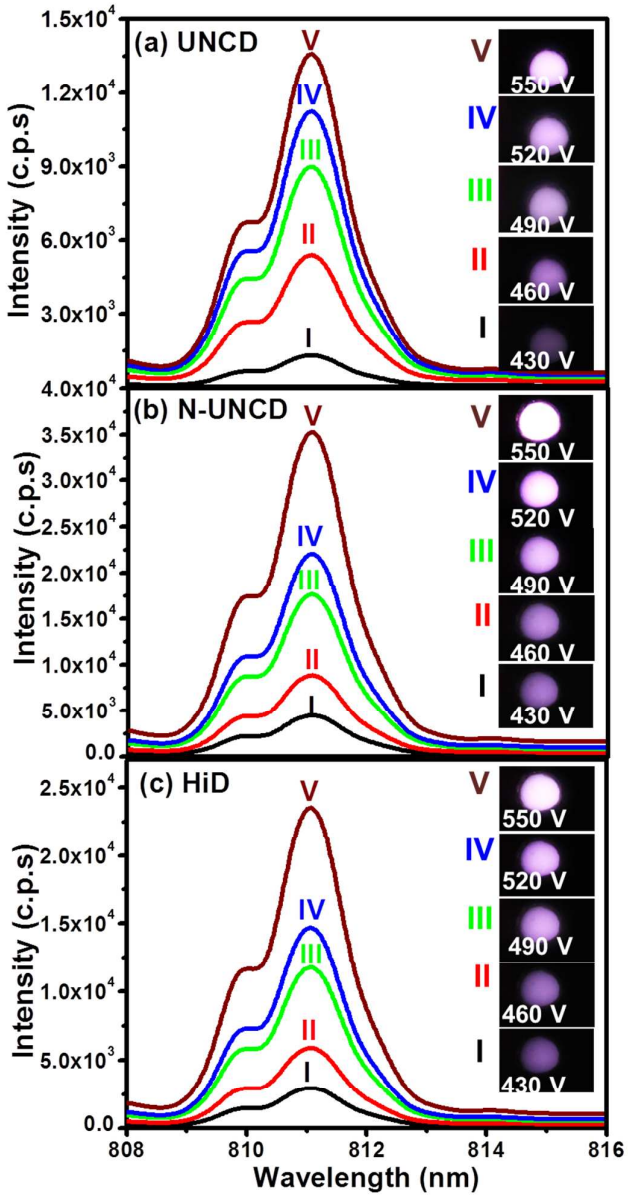

Figure 1. OES of Ar NIR line (811.5 nm) of the microplasma devices, which used (a) UNCD/Au-Si films (b) N-UNCD/Au-Si films and (c) HiD/Au-Si films as cathode. The insets show the corresponding PI images.

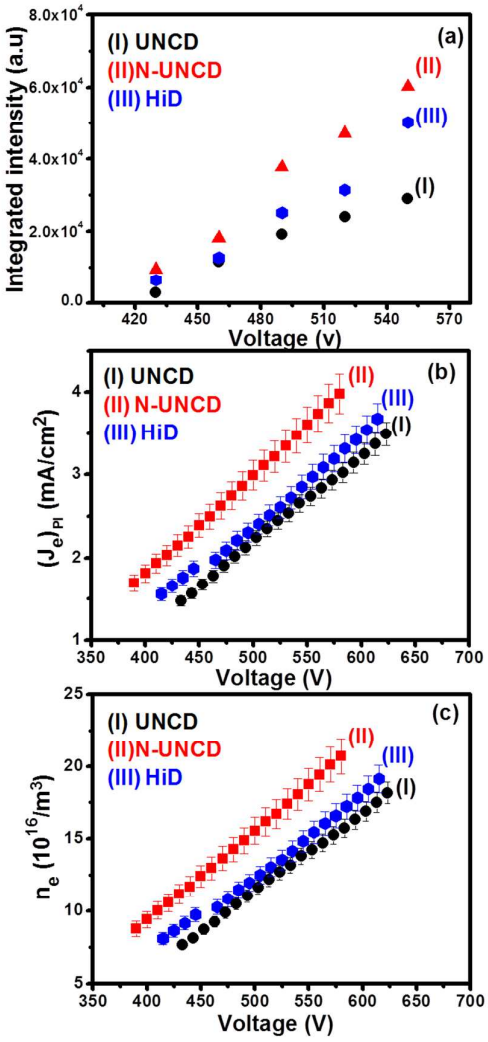

Figure 2. The voltage dependency of (a) Ar NIR (811.5 nm) spectral line intensity, (b) The plasma current density versus applied, $(J_e)_{PI}$-E, characteristics and (c) the plasma density versus applied field, $(n_e)_{PI}$-E, characteristics of the microplasma devices, which used (I) UNCD/Au-Si film, (II) N-UNCD/Au-Si film and (III) HiD/Au-Si films as cathode. [Error bars in the curves depicts the 4-6 % error in experimental data].

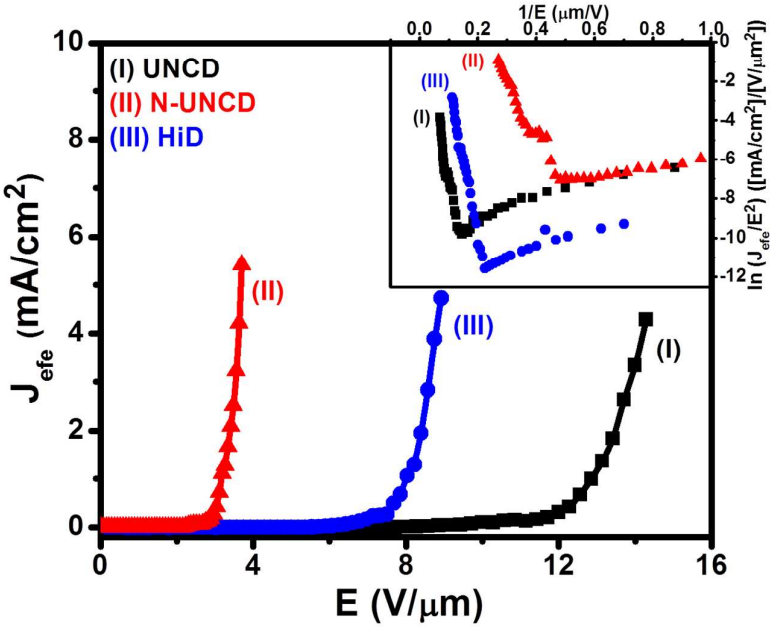

Figure 3. The EFE characteristics, J_{efe}–E properties, of (I) UNCD/Au-Si films, (II) N-UNCD/Au-Si films and (III) HiD/Au-Si films. The inset shows the F-N plots of the UNCD/Au-Si films (curve I), N-UNCD/Au-Si films (curve II) and HiD/Au-Si films (curve III).

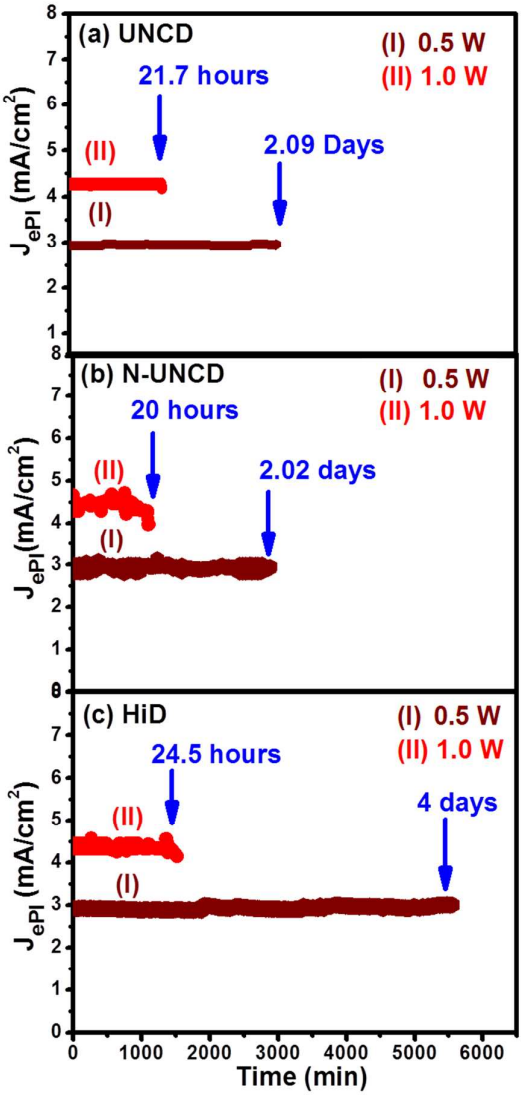

Figure 4. The lifetime measurements in Ar plasma environment with applied DC power of (I) 0.5 and (II) 1 W for the microplasma devices, which used (a) UNCD/Au-Si films, (b) N-UNCD/Au-Si films and (c) HiD/Au-Si films as cathode.

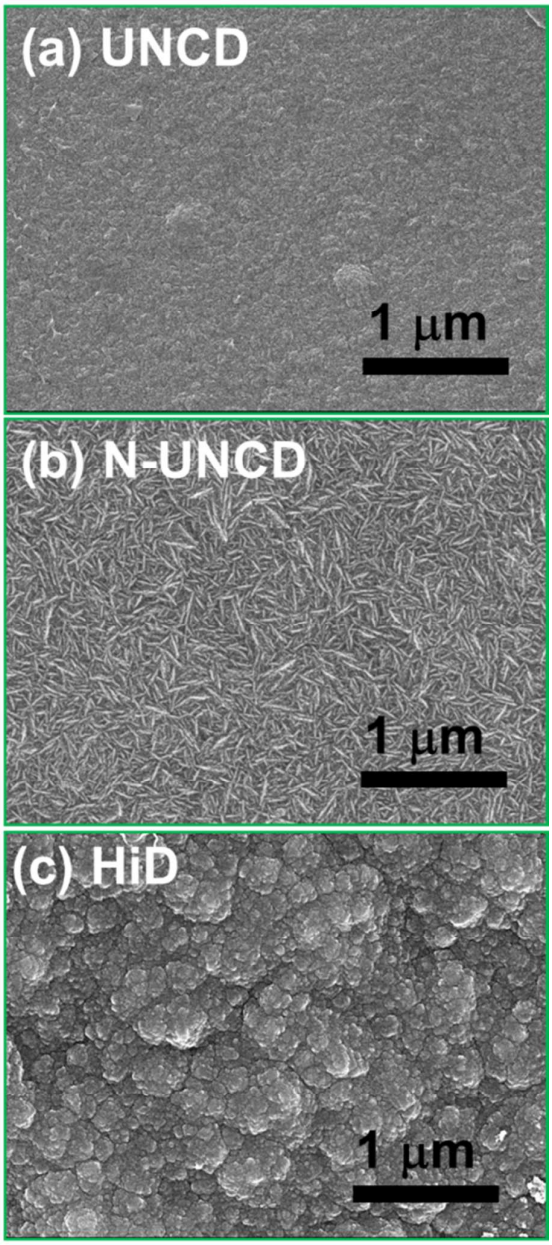

Figure 5. The SEM micrographs of (a) UNCD/Au-Si films, (b) N-UNCD/Au-Si films and (c) HiD/Au-Si films.

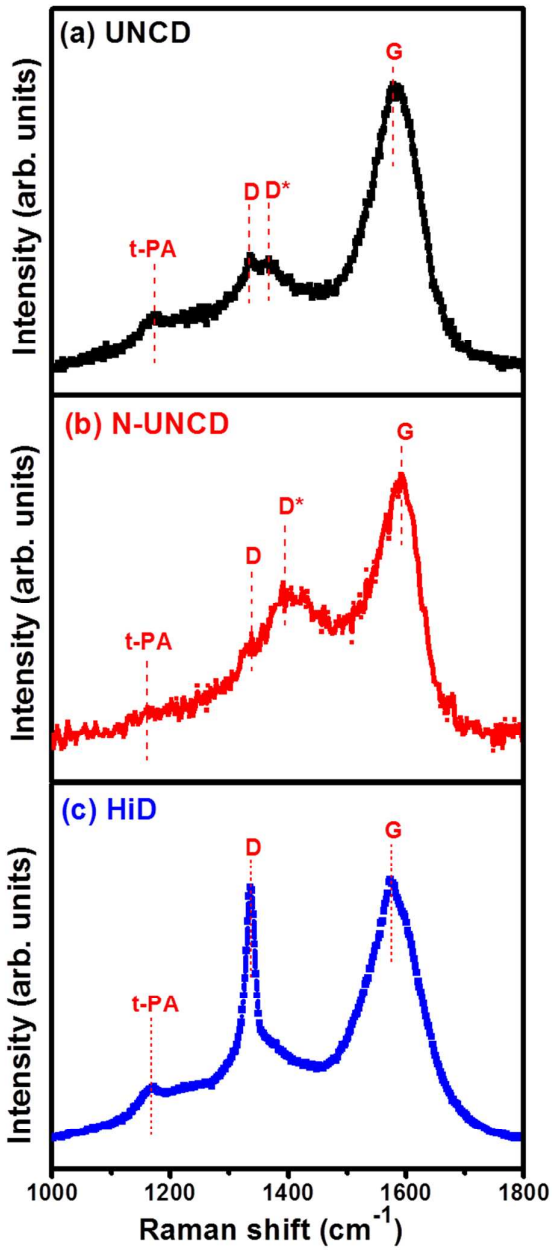

Figure 6. The UV-Raman spectra for (a) UNCD/Au-Si films, (b) N-UNCD/Au-Si films and (c) HiD/Au-Si films.

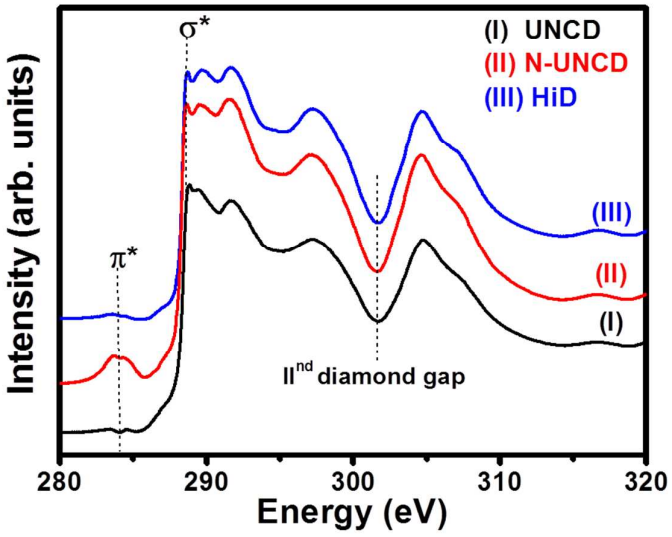

Figure 7. The NEXAFS spectra of (I) UNCD/Au-Si films, (II) N-UNCD/Au-Si films and (III) HiD/Au-Si films.

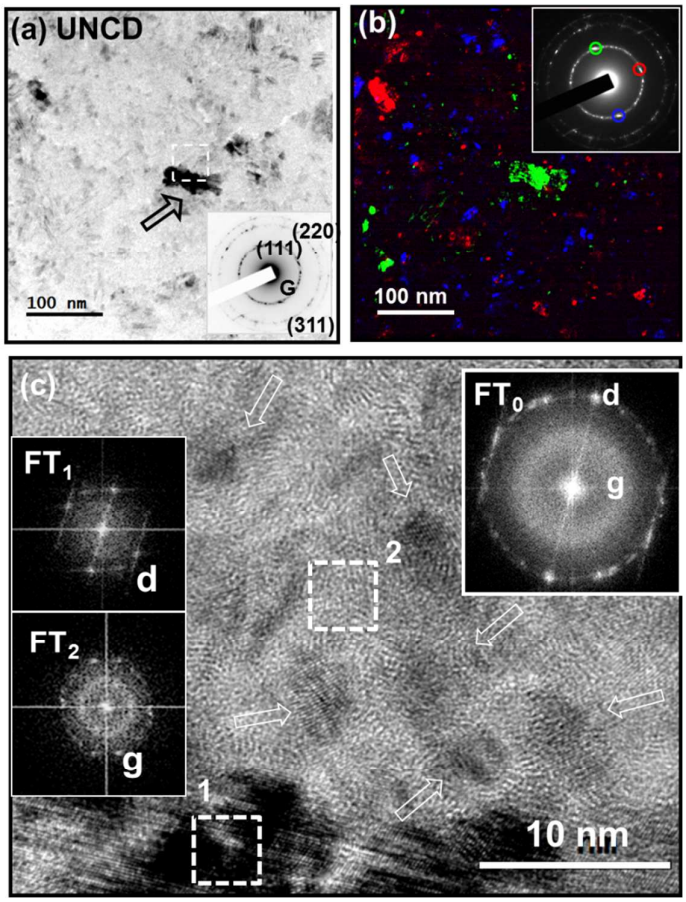

Figure 8. The (a) bright field and (b) composed dark field TEM micrographs of the UNCD/Au-Si films with the inset showing the corresponding SAED. (c) The TEM structure image of the region designated in "a", where the ultra-small diamond grains were designated by arrows. The FT_0 represents the Fourier transformed (FT) diffractogram corresponding to the whole structure image. FT_1 and FT_2 represent the FT image of regions "1" and "2", respectively.

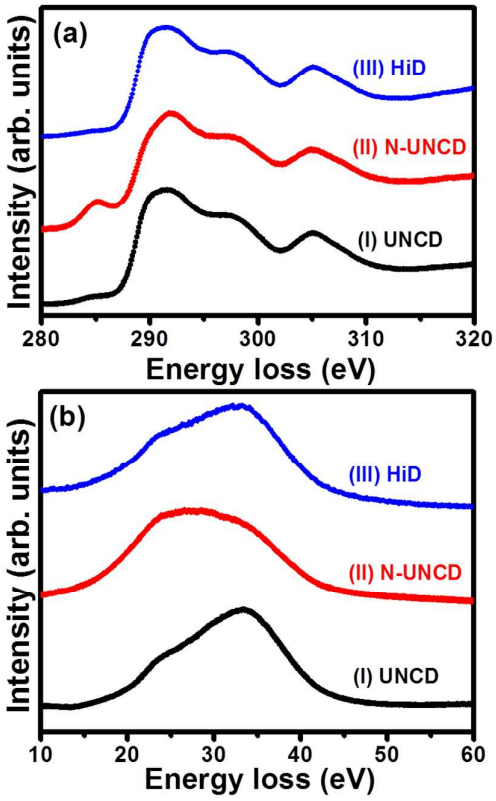

Figure 9. The selected area (a) core-loss and (b) plasmon-loss EELS spectra for (I) UNCD/Au-Si films, (II) N-UNCD/Au-Si films and (III) HiD/Au-Si films.

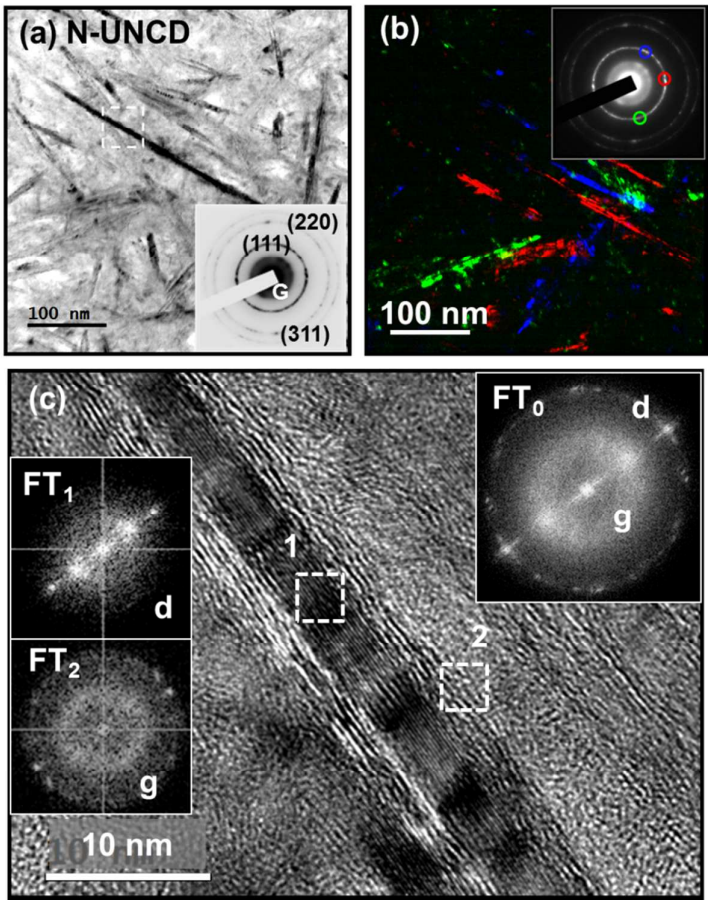

Figure 10. The (a) bright field and (b) composed dark field TEM micrographs of the N-UNCD/Au-Si films with the inset showing the corresponding SAED. (c) The TEM structure image of the region designated in "A", where the FT_0 represents the Fourier transformed diffractogram

corresponding to the whole structure image. FT_1 and FT_2 represent the FT images of regions "1" and "2", respectively.

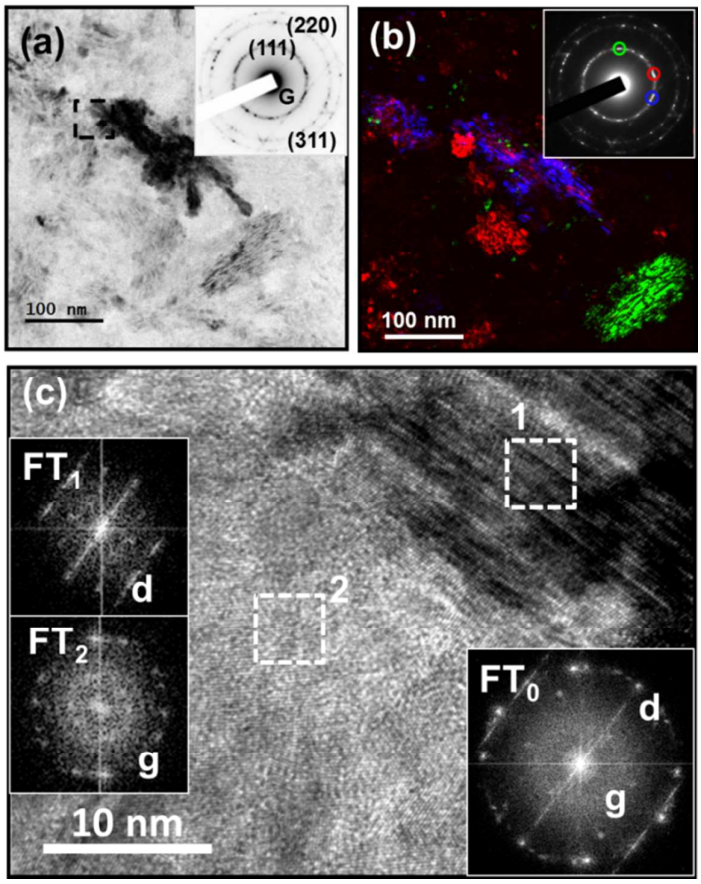

Figure 11. The (a) bright field and (b) composed dark field TEM micrographs of the HiD/Au-Si films with the inset showing the corresponding SAED. (c) The TEM structure image of the region designated in "a", where the FT_0 represents the Fourier transformed diffractogram corresponding to the whole structure image. FT_1 and FT_2 represent the FT images of regions "1" and "2", respectively.

Table of Content

Diamond films are grown on Au coated silicon substrate with different granular structures, which are differentiating in phase compositions and related properties. Microplasma devices are architecture by using these three kinds of diamond films as cathode materials. The plasma illumination properties such plasma current enhanced for the device made with the diamond film, which consists of higher fraction of sp^2 carbon. Plasma characteristics described by optical emission spectrum collected from different applied voltages and corresponding illumination photographs. The robustness of diamond films in microplasma devices tested by estimating lifetime, these results reveals that diamond films with higher fraction of sp^3 carbon exhibits long lifetime.